In Situ Coupling FeM (M = Ni, Co) with Nitrogen-Doped Porous Carbon toward Highly Efficient Trifunctional Electrocatalyst for Overall Water Splitting and Rechargeable Zn–Air Battery

Hai-Xia Zhong, Jun Wang, Qi Zhang, Fanlu Meng, Di Bao, Tong Liu, Xiao-Yang Yang, Zhi-Wen Chang, Jun-Min Yan,* and Xin-Bo Zhang*

Electrocatalysts for hydrogen evolution reaction (HER), oxygen evolution reaction (OER), and oxygen reduction reaction (ORR) are crucial for water splitting and fuel cells/metal–air batteries, of which the benchmark catalysts for HER/ORR and OER are expensive and scarce Pt-based and Ir/Ru-based compounds, respectively. In spite of this, no trifunctional electrocatalyst for HER, OER, and ORR with an acceptable performance have been reported. In response, herein, as a proof-of-concept experiment, this study first in situ couples element abundant FeM (M = Ni, Co) particles with the nitrogen-doped porous carbon (NPC) by a facile and scalable strategy. Unexpectedly, the resulted FeM/NPC exhibits superior trifunctional catalytic activities for HER, OER, and ORR even in the same electrolyte, which can be attributed to the synergistic advantages of FeM/NPC in terms of its good conductivity, highly porous structure, high Brunauer–Emmett–Teller (BET) surface area, nitrogen doping, and the intimate contact of FeM and NPC. Furthermore, such trifunctional catalyst makes the overall water splitting work at moderate overpotential, and endows the assembled Zn–air battery with a good performance and impressive capacity to self-power the overall water splitting, demonstrating its feasibility for practical application.

Dr. H.-X. Zhong, Dr. J. Wang, Q. Zhang, F. L. Meng, Dr. D. Bao, T. Liu,
X.-Y. Yang, Z.-W. Chang, Prof. X.-B. Zhang
State Key Laboratory of Rare Earth Resource Utilization
Changchun Institute of Applied Chemistry
Chinese Academy of Sciences
Changchun 130022, P. R. China
E-mail: xbzhang@ciac.ac.cn
Dr. H.-X. Zhong, T. Liu, Z.-W. Chang
University of Chinese Academy of Sciences
Beijing 100049, China
F. L. Meng, X.-Y. Yang, Prof. J.-M. Yan
Key Laboratory of Automobile Materials
Ministry of Education
and College of Materials Science and Engineering
Jilin University
Changchun 130012, Jilin, P. R. China
E-mail: junminyan@jlu.edu.cn

1. Introduction

Converting decentralized and intermittent energy sources (wind and solar fuel) into the form of H_2 by electrochemical water splitting, and recovering them in fuel cells and rechargeable metal–air batteries holds great promise for the prevalent renewable energy applications, in a large part bypassing the reliance on fossil fuels and thus addressing the resulting energy and environment crisis.[1–8] Impressive progress of these technologies notwithstanding, they face dire challenges centering on the sluggish electrochemical reactions, including oxygen reduction, oxygen evolution, and hydrogen evolution reactions (ORR, OER, and HER), imposing an urgent need for an active catalyst and energy input.[9–16] The state-of-the-art HER and ORR catalysts are Pt-based materials, while these materials are usually poor for OER. Contrarily, RuO_2/IrO_2, as the most active OER catalysts exhibit poor ORR and HER performance. Moreover, their commercialization is seriously limited by high cost, scarcity, and questionable stability.[17–19] Besides this, using different single catalysts needs different equipment and processes at a price of inconvenience and increased cost. Consequently, it is important to develop low-cost and efficient multifunctional electrocatalysts for water splitting and fuel cell/metal–air batteries.

Recently, transition metal (Fe, Co, Ni, Mn)-based electrocatalysts with environmentally friendly nature and high catalytic activities have been widely investigated as promising candidates for ORR, OER, and HER.[20–25] Optimizing the electronic properties of the materials provides an effective way to boost the catalytic activity, such as coupling with a conductive support.[26–28] Particularly, in situ anchoring the metallic catalysts on nitrogen-doped porous carbon (NPC) would be an appealing choice. This is because the close obtained contact between the metallic species and NPC will induce synergistic electronic coupling effects and directly enrich the active sites. Besides, NPC can also effectively promote the dispersity

**ADVANCED
SCIENCE NEWS**
www.advancedsciencenews.com

**ADVANCED
SUSTAINABLE
SYSTEMS**
www.advsustainsys.com

of metallic species and thus enhance the electron/mass-transfer capacity.[29,30] For instance, Dai and co-workers found that both Co_3O_4 on nitrogen-doped graphene and $MnCo_2O_4$/graphene hybrid showed an excellent ORR and OER catalytic activity.[28,31] Simultaneously, Co_xO_y/NC as well as spinel Mn–Co oxide on NCNT (nitrogen doped carbon nanotube) were also explored as the active OER and ORR electrocatalysts.[8,32] In addition, 3d transition metal alloys (FeCo, NiCo, etc.) encapsulated in carbon were also reported to catalyze HER effectively.[33,34] Despite these advantages, utilizing the metallic materials and functional carbon support hybrids is seldom reported for the multifunctional electrocatalysts toward ORR, OER, and HER.[35–38] Therefore, development of low-cost multifunctional electrocatalyst with good ORR, OER, and HER catalytic performance is being actively pursued.

Herein, we develop an in situ coupling FeM (M = Ni, Co) alloy with NPC (FeM/NPC) as a multifunctional electrocatalyst for ORR, OER, and HER via a facile strategy including a solvothermal synthesis of poly(dopamine) (PDA) coated metallic precursor (FeMO/PDA) and the followed carbonization process. Inspiringly, FeM/NPC, with a good conductivity, abundant pores, high Brunauer–Emmett–Teller (BET) surface area, nitrogen doping, and the initial contact between FeM and NPC, displays a positive ORR half-wave potential ($E_{1/2}$), a low OER/HER overpotential and fast kinetics. As a proof-concept application, the water electrolyzer with FeNi/NPC as anode and cathode catalyst shows a cell voltage of 1.63 V at 10 mA cm^{-2}, and the assembled Zn–air battery with FeNi/NPC as the OER and ORR electrocatalyst harvests a low discharge/charge overpotential and good long-term durability. More importantly, this Zn–air battery can self-power the water electrolyzer, highlighting its feasibility of the trifunctional electrocatalyst in the practical application.

2. Results and Discussion

2.1. Structural and Morphological Characterization

The fabrication process is schematically shown in Figure S1 (Supporting Information). Briefly, the synthesis process starts with the dissolution of metal salts and NH_4HCO_3 in a mixed solvent of water and ethanol, followed by the successful polymerization of dopamine, identified by the Fourier transform infrared spectrum (FT-IR) spectra (Figure S2, Supporting Information). And the scanning electron microscopy (SEM) images show FeNiO/PDA and FeCoO/PDA precursors possess particle-like morphology with an average size of 113 and 136 nm, respectively, which are quite smaller than PDA particles (3 µm), suggesting the significance of metallic species (Figures S3a,c and S5a, Supporting Information). After the carbonization, the precursors are directly

converted to FeM/NPC. And X-ray diffraction (XRD) patterns with no discernible impurities in spite of the wide carbon peak at around 27° for FeM/NPC confirm the presence of FeNi and FeCo, which are believed as the active sites (Figure S4, Supporting Information).[20,33,34,39] Similarly, FeNi/NPC and FeCo/NPC have the inherited particle-like morphology except with drastically decreased particle sizes (24 nm for FeNi/NPC and 33 nm for FeCo/NPC; Figure S3, Supporting Information) and rougher surface due to the decomposition of metallic precursors and PDA. Moreover, transmission electron microscopy (TEM) images validate the successful anchoring of FeM alloy particles (25 nm for FeNi/NPC and 50 nm for FeCo/NPC) on the interconnected porous carbon particles (**Figure 1**a,b and Figure S7 (Supporting Information)), benefiting for electron transfer during catalysis process. Accordingly, the observed lattice spaces of 0.208 and 0.201 nm are corresponded to (111) and (110) plane of cubic FeNi and FeCo, respectively, in agreement with the XRD results. Furthermore, high-angle annular dark field scanning transmission electron microscopy (HADDF-STEM) analysis is performed to probe the spatial distribution of the constituent elements (Figure 1c–i and Figure S8 (Supporting Information)). STEM images further verified that various metallic alloy particles are coupled with the aggregated carbon particles for FeM/NPC, which are uniformly overlapped by Fe and M (Ni, Co) element. Meanwhile, C, N, and O are evenly distributed throughout the whole structure. Of note, the observation of O is ascribed to the easy partial oxidation of FeNi without the carbon coating and the absorption of oxygen or water of the porous carbon under air atmosphere.
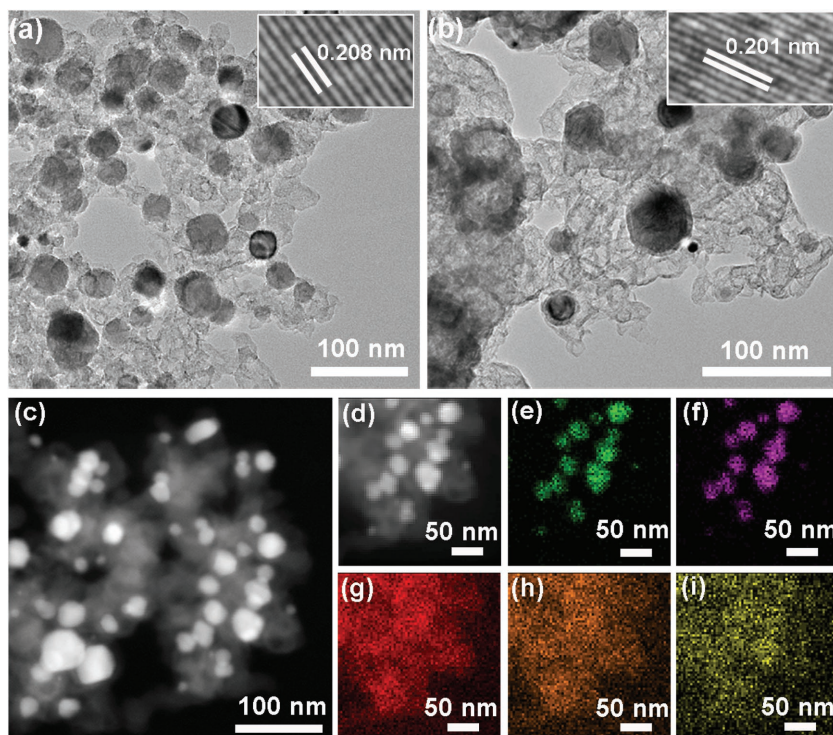

Figure 1. TEM images of a) FeNi/NPC and b) FeCo/NPC (inset: the corresponding high-resolution TEM images); c,d) HADDF-STEM images of FeNi/NPC; the corresponding element mapping images of e) Fe, f) Ni, g) C, h) N, and i) O.

**ADVANCED
SCIENCE NEWS**

www.advancedsciencenews.com

**ADVANCED
SUSTAINABLE
SYSTEMS**

www.advsustainsys.com

The porous nature of FeM/NPC is analyzed by the nitrogen sorption measurements. Typically, the distinct hysteresis loop ($\approx$0.45–1.0 P/P_0) implies the existences of mesopore, which is favorable for mass transport at FeM/NPC electrode (**Figure 2**a and Figure S9c (Supporting Information)).[40,41] The pore distribution curves further disclose their average pore size (11 nm for FeNi/NPC and 14 nm for FeCo/NPC; Figure 2a and Figure S9d (Supporting Information)). Higher BET surface areas are achieved by FeNi/NPC (426 m^2 g^{-1}) and FeCo/NPC (475 m^2 g^{-1}) compared to their corresponding precursors (78.4 and 46.6 m^2 g^{-1}), respectively, which is owing to the decomposition of the metallic precursor and PDA (Figure S10, Supporting Information). In addition, the defect structure is investigated by Raman spectra. As shown in Figure 2b, two remarkable peaks at 1345 and 1600 cm^{-1} are founded for FeM/NPC, which are attributable to the typical D and G band, respectively.[42] Note that the I_D/I_G values of FeNi/NPC (1.03) and FeCo/NPC (1.01) are similar and higher than that of NPC

(0.87), indicating the important role of the metallic species in generating more defects in FeM/NPC.

To probe the chemical structure of the samples, X-ray photoelectron spectroscopy (XPS) measurements are performed. The high-resolution spectrum of C 1s for FeM/NPC can be deconvoluted into four peaks: C=C (284.6 eV), C=N (285.2 eV), C—O (286.1 eV), and O=C—OH (288.5 eV, Figure 2c), suggesting the successful nitrogen doping into the carbon framework;[43,44] and three species are discovered in the fitted high-resolution N 1s peaks (Figure 2d): pyridinic-N (N1, 398.6 eV), pyrrolic-N (N2, 399.9 eV), and graphitic-N (N3, 401.1 eV).[43,45] With the increase in the pyrolysis temperatures, the content of pyrrolic-N for FeNi/NPC is decreased due to its instability at high temperature (Figure 2d and Figure S11d (Supporting Information)). As a result, N1 and N3, which are well-known OER and ORR active sites,[20] are dominated in FeM/NPC. Note that metal oxides are also observed in the high-resolution XPS spectra of Fe 2p$_{3/2}$, Co 2p$_{3/2}$, and Ni 2p$_{3/2}$ owing to the partial oxidation of FeM alloy under air atmosphere (Figure 2d,e), wherein 1.29% and 0.95% of Fe and Ni are observed for FeNi/NPC, and 0.85% and 0.61% of Fe and Co are observed for FeCo/NPC, respectively.[46–50] Thus, it can be presumed that both active FeM species and nitrogen doping would be the active materials to catalyze ORR, OER, and HER.
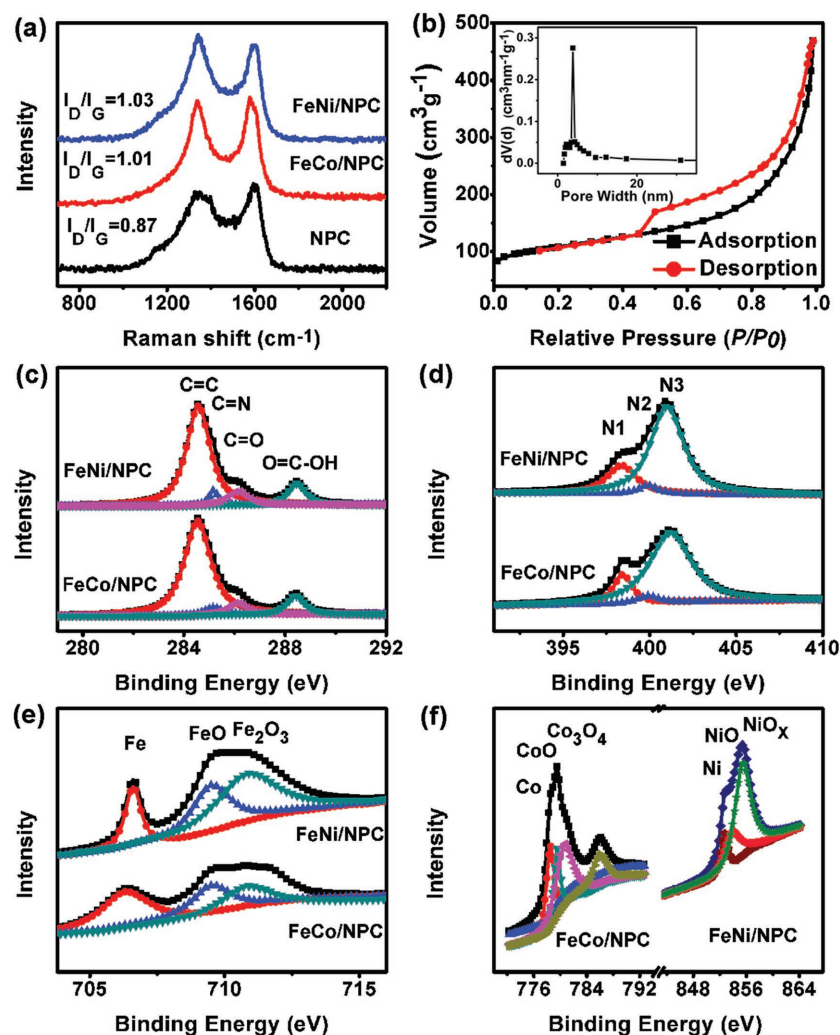
2.2. Electrocatalytic Performance of ORR, OER, and HER

The ORR catalytic activities of FeM/NPC are investigated by the rotating disk electrode (RDE) technique. For comparison, the ORR performances of FeNi, FeCo, NPC, the physical mixtures of FeM and NPC (FeNi+NPC, FeCo+NPC), and commercial Pt/C are also evaluated. As displayed in Figure S13 (Supporting Information), a well-defined cathodic peak of FeM/NPC emerges in the cyclic voltammetry (CV) curve in the O$_2$-saturated electrolyte and is quite different from the featureless one in N$_2$-saturated electrolyte, pronouncing their ORR catalytic activities. The ORR polarization curves (**Figure 3**a and Figure S15a (Supporting Information)) show that FeCo+NPC (0.58 V) and FeNi+NPC (0.46 V) exhibit a more positive $E_{1/2}$ compared to their support-free counterparts (0.39 V for FeCo and 0.42 V for FeNi) owing to the improved electron-transfer kinetics. Albeit with a high conductivity and BET surface (627 m^2 g^{-1}), NPC still has a negative $E_{1/2}$ (0.58 V) because of the deficient active sites. Taking the advantages of NPC and FeM, FeCo/NPC and FeNi/NPC harvest better $E_{1/2}$, which are even close to that of the commercial Pt/C (0.85 V; Figure 3a and Table S1 (Supporting Information)), implying the

Figure 2. a) Raman spectra of NPC, FeNi/NPC, and FeCo/NPC; b) N$_2$ adsorption–desorption isotherm curves of FeNi/NPC (inset: the corresponding pore size distribution); high-resolution c) C 1s, d) N 1s, e) Fe 2p$_{3/2}$, and f) Co 2p$_{3/2}$ and Ni 2p$_{3/2}$ XPS spectra of FeNi/NPC and FeCo/NPC.

ADVANCED
SCIENCE NEWS
www.advancedsciencenews.com

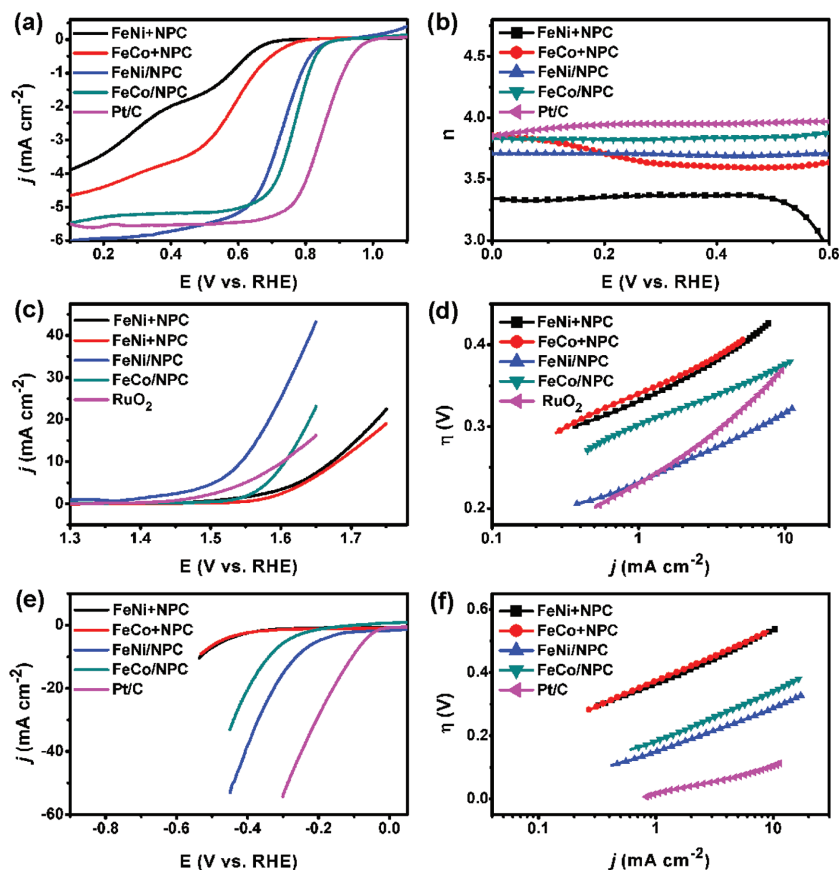ADVANCED
SUSTAINABLE
SYSTEMS
www.advsustainsys.com

Figure 3. a) ORR polarization curves, b) electron-transfer number at various potentials, e) HER polarization curves and f) the corresponding Tafel plots of FeNi+NPC, FeCo+NPC, FeNi/NPC, FeCo/NPC, and Pt/C in 0.1 M KOH; c) OER polarization curves and d) Tafel plots of FeNi+NPC, FeCo+NPC, NPC, FeNi/NPC, FeCo/NPC, and RuO$_2$ in 0.1 M KOH.

importance of in situ anchoring of FeM on NPC. The superior ORR catalytic activity of FeM/NPC mainly originates from the rich active components (FeM and nitrogen doping carbon),[4,8] good conductivities, abundant pores, and the intimate contact between FeM and NPC. Interestingly, a well-defined plateau of the diffusion-limiting currents in the ORR polarization curves are acquired by FeNi/NPC and FeCo/NPC, representing the diffusion-controlled process with an efficient 4e$^-$ dominated ORR pathway.[45,51] To gain a deep insight into the ORR kinetics, the kinetic parameter is analyzed by the Koutecky–Levich (K–L) plots. The near linearity of the K–L plots and a parallelism of the fitting lines suggest the first-order reaction kinetics with regard to the concentration of dissolved oxygen and similar electron-transfer numbers (n) at various potentials for FeM/NPC electrodes (Figures S16–S18, Supporting Information).[28,52–54] Accordingly, the average electron-transfer numbers (n) are calculated to be 3.8 for FeNi/NPC and 3.85 for FeCo/NPC, further indicating a 4e$^-$ dominant ORR catalytic process at FeM/NPC electrode. However, n for FeNi, FeCo, NPC, FeNi+NPC, and FeCo+NPC is only 3.02, 3.56, 3.08, 3.4, and 3.65 based on the K–L results, respectively, which are associated with an apparent existence of 2e$^-$ ORR catalytic pathway with generating more peroxide (HO$_2^-$) compared to FeCo/NPC and FeNi/NPC. Therefore, a rotating ring disk electrode (RRDE) technique

is carried out to monitor the generation of HO$_2^-$ during the ORR process. The yields of HO$_2^-$ for FeCo/NPC and FeNi/NPC are less than 10%, giving n of 3.83 and 3.8 (Figure 3b and Figure S19 and Table S1 (Supporting Information)), respectively, which are consistent with the RDE results. Unfortunately, higher yields of HO$_2^-$ are detected by FeNi (44.6%), FeCo (19.8%), NPC (33.9%), FeNi+NPC (31.4%), and FeCo+NPC (15.3%), giving n of 3.11, 3.6, 3.32, 3.37, and 3.69, respectively, further demonstrating the superior ORR catalytic activity of FeM/NPC.[51]

The OER and HER electrocatalytic activities for FeM/NPC are also evaluated by RDE technique in 0.1 M KOH. For comparison, the OER performance of RuO$_2$ and HER performance of Pt/C are also tested. Obviously, FeNi+NPC and FeCo+NPC exhibit a smaller OER overpotential (0.44 and 0.45 V, respectively) at 10 mA cm^{-2} compared to FeNi (0.46 V), FeCo (0.5 V), and NPC (0.53 V) due to the improved electron-charge transfer (Figure S23, Supporting Information). However, fewer improvements in the overpotential and current density imply the intrinsic active material (FeM) is very important in determining the catalytic performance. Inspiringly, the targeted FeNi/NPC and FeCo/NPC exhibit a comparable overpotential of 0.31 and 0.36 V compared to that for RuO$_2$ (0.36 V), respectively, further confirming the importance of the active components (FeM and nitrogen doping) and the initial contact of each component, as well as the good conductivity and pore structure. Furthermore, the superior OER performance of FeNi/NPC and FeCo/NPC is gleaned from their smaller Tafel slopes (62 and 70 mV dec^{-1}, respectively) than that for FeNi (90 mV dec^{-1}), FeCo (92 mV dec^{-1}), NPC (97 mV dec^{-1}), FeNi+NPC (80 mV dec^{-1}), and FeCo+NPC (85 mV dec^{-1}), which even outperforms the commercial RuO$_2$ (88 mV dec^{-1}), implying their faster OER kinetics (Figure 3d and Figure S15d and Table S1 (Supporting Information)) and a chemical step following the first electron-transfer step as the rate-determining step at FeM/NPC electrode.[55–57] In addition, their HER activities are shown in Figure 3e,f and Figure S15e,f (Supporting Information). Undoubtedly, electrocatalysis HER at the commercial Pt/C electrode starts at low cathodic potential and the current increases sharply, corresponding to a overpotential of 110 mV at 10 mA cm^{-2}. Similarly, FeNi/NPC also achieves a small operating overpotential (260 mV) at identical current density, beyond which the cathodic current increases rapidly. Within the catalyst series, the overpotential at 10 mA cm^{-2} increases in the order: FeNi/NPC (260 mV) < FeCoNPC (340 mV) < FeNi+NPC (520 mV) < FeCo+NPC (530 mV) < FeNi (590 mV) < NPC (640 mV) < FeCo (700 mV), suggesting the superior HER catalytic activity at FeM/NPC electrodes. Similarly, a faster HER kinetic at FeM/NPC electrode is observed as indicated by the smaller Tafel
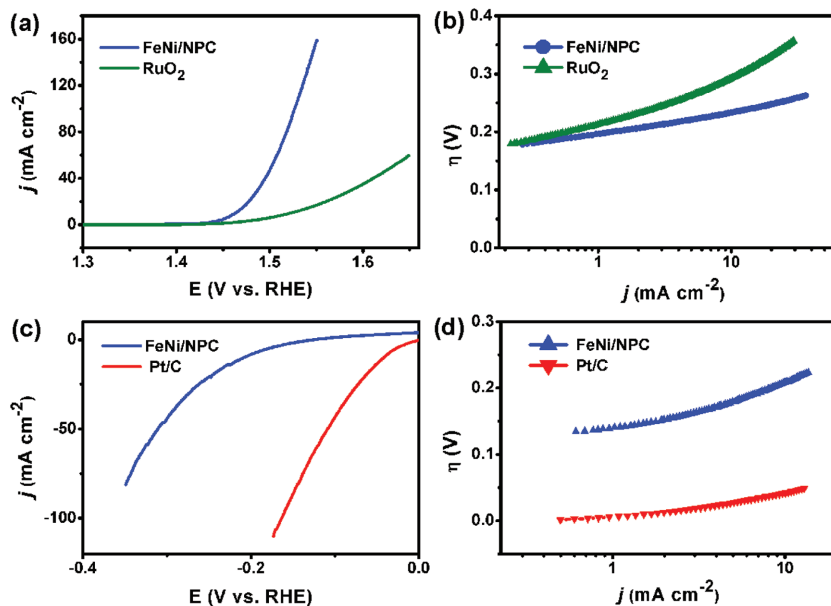
**ADVANCED
SCIENCE NEWS**

www.advancedsciencenews.com

**ADVANCED
SUSTAINABLE
SYSTEMS**

www.advsustainsys.com

Figure 4. a,b) OER polarization curves and Tafel plots of FeNi/NPC and RuO_2 on carbon paper in 1 M KOH; c,d) HER polarization curves and Tafel plots of FeNi/NPC and Pt/C in 1 M KOH.

slope (112 and 125 mV dec^{-1} for FeNi/NPC and FeCo/NPC, respectively), along with a possible Volmer–Heyrovsky reaction pathway and the electrochemical desorption of hydrogen as the rate-limiting step.[58,59] To further identify the significant role of FeM in determining the catalytic activity, SCN^- poison experiments are performed (Figure S24, Supporting Information). When introducing SCN^-, great current density losses are observed for FeM/NPC electrodes, which are likely because some of the metallic active sites are covered due to the strong interaction of the metallic species and SCN^-, identifying the great contribution of FeM to the enhanced catalytic activities of FeM/NPC.

The OER and HER catalytic activities are also investigated in 1 M KOH with the catalyst coated carbon paper as working electrode. As displayed in **Figure 4**a, FeNi/NPC only needs 1.46 V to deliver an anodic current density of 10 mA cm^{-2}, surpassing over the commercial RuO_2 (1.51 V). Moreover, a smaller Tafel slope (35 mV dec^{-1}) is harvested by FeNi/NPC compared to that of the commercial RuO_2 (62 mV dec^{-1}), enabling it one of the most active OER catalysts in the alkaline electrolyte (Figure 4b). Likewise, a good HER catalytic activity with a small overpotential (200 mV) at 10 mA cm^{-2} and Tafel slope of 40 mV dec^{-1} are obtained by FeNi/NPC electrode (Figure 4c,d), which is very close to these of Pt/C (40 mV and 30 mV dec^{-1}). Therefore, FeM/NPC, arming with a high OER and HER performance, could be the promising dual catalyst for water splitting.

2.3. Overall Water Splitting Performance

As a proof-concept application, an electrolyzer in a two-electrode setup using FeNi/NPC as the anode and cathode electrocatalysts is made (**Figure 5**). For well comparison, we also make

an electrolyzer with the mixture of Pt/C and RuO_2 (Pt/C-RuO_2) as both anode and cathode electrocatalysts. Importantly, the observed voltage of the water electrolyzer with FeNi/NPC is 1.63 V at 10 mA cm^{-2}, which is comparable to the one with Pt/C-RuO_2 (1.58 V, Figure 5b). Aside from the comparable activity, a better long-term durability is achieved by FeNi/NPC as only slight voltage change emerges after 10 h continuous water electrolysis owing to the stable structure with no obvious phase change of the catalyst, indicated by the XRD patterns (Figures S4 and S25, Supporting Information). However, the Pt/C and RuO_2 electrodes compromise the continuous water splitting along with a dramatically increased overpotential. Additionally, the agreement of the theoretically calculated and experimentally monitored gas reveals that the Faradic efficiency of FeNi/NPC electrode is close to 100%, wherein the small loss is likely due to the dissolved gas in the electrolyte and the attached bubbles on the electrode surface. Moreover, gas chromatograms and mass spectrum further confirm that the product gases are only composed of H_2 and O_2 (Figures S26 and S27, Supporting Information). Additionally, an apparent gas bubbling is observed for the water electrolysis drived by a single-cell AAA battery with a nominal voltage of 1.5 V (Figure 5d), further demonstrating the bifunctionality of the FeNi/NPC for the overall water splitting in the alkaline medium. Therefore, FeNi/NC electrode is enforceable in the alkaline electrolyzer with a comparable OER and HER catalytic activity but a better long-term durability.

2.4. Zn–Air Battery Performance

As another proof-concept application toward OER and ORR, Zn–air battery with FeNi/NPC as the air electrode is assembled and operated in an ambient condition using atmospheric air instead of purging oxygen. For the primary battery, the Zn foil is continuous consumed since the discharge starts. And the battery finally ceases when the Zn metal is completely depleted, giving a specific capacity of 800 mAh g^{-1} normalized to the consumed Zn mass (**Figure 6**a). To further demonstrate the bifunctional electrocatalytic activity (ORR and OER) of FeNi/NPC, the performance of a recharge Zn–air battery is evaluated. As shown in Figure 6b, such a battery affords a discharge voltage of 1.15 V and a charge voltage of 1.94 V at the current density of 25 mA cm^{-2}, which are comparable to the discharge voltage of Pt/C (1.21 V) and the charge voltage of RuO_2 (1.98 V) at the same current density. On the other sides, FeNi/NPC greatly outperforms RuO_2 and Pt/C with respect to the discharge voltage (1.04 V) and the charge voltage (2.49 V), indicating its excellent bifunctional electrocatalytic activity toward ORR and OER. Besides, the battery with FeNi/NPC exhibits almost no obvious changes of the discharge and charge voltage after 150 continuous charge and discharge cycles, whereas a gradual
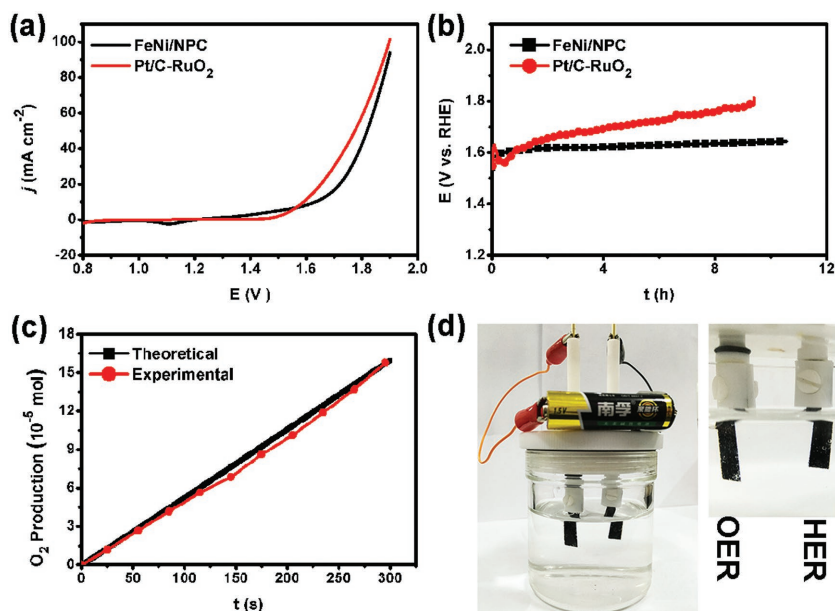
**ADVANCED
SCIENCE NEWS**
www.advancedsciencenews.com

**ADVANCED
SUSTAINABLE
SYSTEMS**
www.advsustainsys.com

Figure 5. a) Polarization curve of the overall water splitting with FeNi/NPC and Pt/C-RuO$_2$ as both anode and cathode in 1 M KOH; b) the corresponding chronopotentiometric response at 10 mA cm^{-2}; c) the amount of theoretically calculated and experimentally measured gaseous products versus time for the water electrolyzer with FeNi/NPC as the anode and cathode in 1 M KOH solution; d) demonstration of the overall water splitting powered by an AAA battery with a nominal voltage of 1.5 V with FeNi/NPC electrodes.
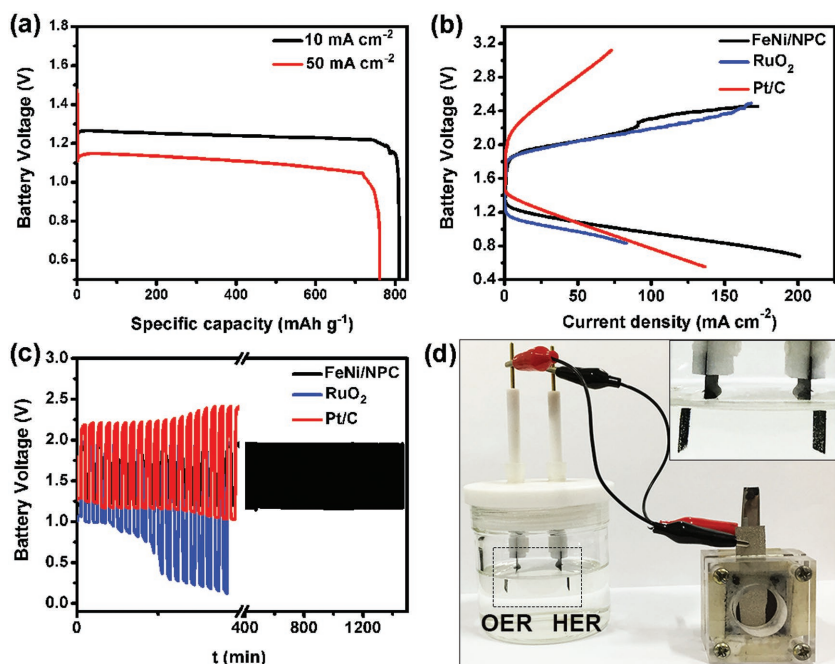

Figure 6. a) Typical discharge curves of primary Zn–air batteries with FeNi/NPC as the air electrode under a continuous discharge until the complete consumption of Zn at two different current densities (specific capacity was normalized to the mass of consumed Zn); b) charge and discharge polarization curves of Zn–air batteries with Pt/C, RuO$_2$, and FeNi/NPC as air electrode, respectively; c) charge and discharge cycling curves of Zn–air batteries with Pt/C, RuO$_2$, and FeNi/NPC as the air electrodes; d) demonstration of the overall water splitting powered by the Zn–air battery with FeNi/NPC as the HER, OER, and ORR catalysts.

increase in the charge voltage and a decrease in the discharge voltage are observed for Pt/C since the test starts (Figure 6c). Meanwhile, RuO$_2$ shows a dramatical loss in the discharge voltage after 10 cycles, revealing the better stability of FeNi/NPC. Importantly, the Zn–air battery can also self-power the overall water splitting with FeNi/NPC as the multiple functional electrocatalysts (Figure 6d), highlighting the trifuntional electrocatalyst feasiblity of FeM/NPC in the practical application. Moreover, a single Zn–air battery can power a small air fan and a light-emitting diode can be given out light powered by the stack with two Zn–air batteries and keeps it shining at least one week (Figure S31, Supporting Information). Therefore, as trifunctional electrocatalyst, FeNi/NPC demonstrates its superiority in the system combining the water splitting with a Zn–air battery.

3. Conclusion

In summary, FeNi and FeCo alloys are in situ coupled with NPC via a facile and scalable strategy, wherein NPC cannot only increase the dispersity of the metallic species and thus promote the electron transfer, but also afford complementary active sites for enhancing the catalytic activity. Benefiting from a good electron conductivity, high BET surface, plentiful pores, and active sites, as well as the close connection of FeM and NPC, FeM/NPC exhibits a positive ORR $E_{1/2}$, low OER, and HER overpotential and the according fast kinetics. More importantly, such an electrocatalyst facilitates the overall water splitting in a convenient and moderate way and the assembled Zn–air battery operate at low charge/discharge overpotential with a long cycle lifetime. Moreover, such a Zn–air battery can self-power the overall water splitting, greatly reducing the production cost and highlighting its practicability. It is anticipated that this facile and scalable stratagem can be expanded to obtain other alloy on heteroatom-doped porous carbon and this FeM/NPC can be applied in the other fields, such as for Li-ion batteries and supercapacitors.

4. Experimental Section

Synthesis of FeNi/NPC: NiCl$_2$.6H$_2$O (1 mmol), FeCl$_3$.6H$_2$O (1 mmol), and 10 mmol of NH$_4$HCO$_3$ was dissolved in the mixed solvent of water (30 mL) and ethanol (15 mL) by a ultrasonication and vigorously stirring at room temperature for 2 h.

**ADVANCED
SCIENCE NEWS**

www.advancedsciencenews.com

**ADVANCED
SUSTAINABLE
SYSTEMS**

www.advsustainsys.com

Afterward, 1.2 g of dopamine was added and the obtained solution was heated at 50 °C for 24 h. Subsequently, the black powder was obtained by filtrating, washing with water and freeze drying. Finally, this powder was calcinated at 800 °C for 2 h under Ar atmosphere and 800 °C for 1 h under NH_3/Ar (V_{NH_3}/V_{Ar} = 33.3%/66.7%) atmosphere. FeCo/NPC was synthesized by the same procedure of FeNi/NPC except that $CoCl_2.6H_2O$ replaced $NiCl_2.6H_2O$. To investigate the effects of pyrolysis temperature on catalytic performance, the first pyrolysis temperatures were varied (700, 800, and 900 °C).

Characterization and Electrochemical Measurements: Powder XRD measurements were measured on Bruker D8 Focus Powder X-ray diffractometer using Cu Kα radiation (40 kV, 40 mA). TEM was performed using a FEI Tecnai G_2 S-Twin instrument with a field emission gun operating at 200 kV. Raman spectra were collected with a Renishaw 2000 model confocal microscopy Raman spectrometer with a CCD (charge-coupled device) detector and a holographic notch filter at ambient conditions. FT-IR tests were performed on a Nicolet 6700 spectrometer equipped with attenuated total reflectance sample holder. The porosity was detected by nitrogen sorption using a Micromeritics ASAP 2020 analyzer. Thermogravimetric analysis was performed under Ar atmosphere by 5 °C min^{-1} on a NETZSCH STA 449 F3 Simultaneous TGA-DSC Instrument. XPS spectra were collected with an ESCALAB MK II X-ray photoelectron spectrometer using an Al Kα source. All electrochemical measurements were conducted on a BioLogic VMP3 electrochemical workstation. The RDE and RRDE experiments were performed on a modulated speed electrode rotator (MSR) electrode rotator (Pine Instrument Co.). Mass analysis of the generated gases was performed using an Ominstar-Thermostar GSD 320 system (Pfeiffer Vacuum) mass spectrometer, wherein Ar was chosen as the carrier gas. A Techcomp GC7900 gas chromatograph with a thermal conductivity detector was also used to analyze the gas products generated.

The electrochemical tests were conducted in a three-electrode cell in 0.1 M KOH, wherein RDE or RRDE, Ag/AgCl electrode, and Pt mesh were serviced as the working electrode, reference electrode, and counter electrode, respectively. Before each test, RDE (5.0 mm in diameter) or RRDE (5.61 mm in diameter) was polished by the alumina slurries (1 μm and 0.05 μm), and washed with water and ethanol by sonicating. Catalysts (10 mg) were dispersed into 1 mL of ethanol and 50 μL of Nafion solution by a sonication for 30 min. Then, the catalyst inks were drop-casted on RDE with a catalyst loading of 0.485 mg cm^{-2}. For RuO_2, XR-72 carbon (RuO_2/XR-72: 10 mg/2 mg) was introducing to ensure a good conductivity of the electrocatalyst.

As for ORR, CV tests were conducted in N_2- and O_2-saturated 0.1 M KOH solution from −1.0 V to 0.2 V with a scan rate of 50 mV s^{-1}. RDE measurements were carried out in an O_2-saturated 0.1 M KOH solution with a scan rate of 5 mV s^{-1} and the different rotating speeds (400–2025 rpm). RRDE measurements were conducted in an O_2-saturated 0.1 M KOH solution with a scan rate of 5 mV s^{-1} and a rotating speed of 1600 rpm, and the ring potential was constant at 0.5 V. With respect to OER, CV tests were conducted in an O_2-saturated 0.1 M KOH solution from 0 V to 0.7 V with a scan rate of 5 mV s^{-1} and a rotating speed of 1600 rpm. As for HER, CV tests were conducted in an N_2-saturated 0.1 M KOH solution from −1.4 to −0.8 V with a scan rate of 5 mV s^{-1} and a rotating speed of 1600 rpm. And the impedance was tested by electrochemical impedance spectroscopy measurements with an AC voltage with 10 mV amplitude in a frequency range from 100 kHz to 0.1 Hz at 0. 5 V. The OER and HER performance is also investigated in 1 M KOH, wherein the carbon paper loading with the catalyst (0.6 mg cm^{-2}), a graphite rod and the saturated calomel electrode is serviced as the working electrode, counter electrode, and reference electrode, respectively. And Pt/C-RuO_2 electrode is obtained by loading the Pt/C and RuO_2 (mass ratio: 1/1) on the carbon paper. During the chronoamperometric measurement, the generated gas is monitor by a gas burette. All potentials were iR-compensated to 85% with the built-in program and converted to a reversible hydrogen electrode scale via the calibration. And the presented current density was normalized to the geometric surface area.

The Zn–air battery test was conducted in a homemade battery, where catalysts coated carbon paper and Zn plate were used as the air electrode and anode, respectively. The catalyst loading was 1 mg cm^{-2} and 6 M KOH solution containing 0.2 M zinc acetate was used as the electrolyte. Cycling test was conducted by one discharge step (10 mA cm^{-2} for 5 min) followed by a charge step for the same current and time.

Supporting Information

Supporting Information is available from the Wiley Online Library or from the author.

Acknowledgements

Conflict of Interest

The authors declare no conflict of interest.

Keywords

[1] J. Chow, R. J. Kopp, P. R. Portney, *Science* **2003**, *302*, 1528.

[2] M. S. Faber, R. Dziedzic, M. A. Lukowski, N. S. Kaiser, Q. Ding, S. Jin, *J. Am. Chem. Soc.* **2014**, *136*, 10053.

[3] R. D. Smith, M. S. Prevot, R. D. Fagan, Z. Zhang, P. A. Sedach, M. K. Siu, S. Trudel, C. P. Berlinguette, *Science* **2013**, *340*, 60.

[4] Y. Zhu, W. Zhou, Y. Chen, J. Yu, M. Liu, Z. Shao, *Adv. Mater.* **2015**, *27*, 7150.

[5] T. Y. Ma, J. Ran, S. Dai, M. Jaroniec, S. Z. Qiao, *Angew. Chem., Int. Ed.* **2015**, *54*, 4646.

[6] E. Proietti, F. Jaouen, M. Lefevre, N. Larouche, J. Tian, J. Herranz, J. P. Dodelet, *Nat. Commun.* **2011**, *2*, 416.

[7] R. Wu, J. Zhang, Y. Shi, D. Liu, B. Zhang, *J. Am. Chem. Soc.* **2015**, *137*, 6983.

[8] A. Zhao, J. Masa, W. Xia, A. Maljusch, M. G. Willinger, G. Clavel, K. Xie, R. Schlogl, W. Schuhmann, M. Muhler, *J. Am. Chem. Soc.* **2014**, *136*, 7551.

[9] Y. Gorlin, T. F. Jaramillo, *J. Am. Chem. Soc.* **2010**, *132*, 13612.

[10] C. C. McCrory, S. Jung, I. M. Ferrer, S. M. Chatman, J. C. Peters, T. F. Jaramillo, *J. Am. Chem. Soc.* **2015**, *137*, 4347.

[11] C. C. McCrory, S. Jung, J. C. Peters, T. F. Jaramillo, *J. Am. Chem. Soc.* **2013**, *135*, 16977.

[12] G. Wu, P. Zelenay, *Acc. Chem. Res.* **2013**, *46*, 1878.

[13] Q. Lu, Y. Yu, Q. Ma, B. Chen, H. Zhang, *Adv. Mater.* **2016**, *28*, 1917.

[14] Z. Fan, Z. Luo, X. Huang, B. Li, Y. Chen, J. Wang, Y. Hu, H. Zhang, *J. Am. Chem. Soc.* **2016**, *138*, 1414.

[15] C. Tan, H. Zhang, *Chem. Soc. Rev.* **2015**, *44*, 2713.

**ADVANCED
SCIENCE NEWS**

www.advancedsciencenews.com

**ADVANCED
SUSTAINABLE
SYSTEMS**

www.advsustainsys.com

[16] H. Zhang, *ACS Nano* **2015**, *10*, 9451.

[17] S. Chen, J. Duan, M. Jaroniec, S. Z. Qiao, *Angew. Chem., Int. Ed.* **2013**, *52*, 13567.

[18] Z. Shan, P. S. Archana, G. Shen, A. Gupta, M. G. Bakker, S. Pan, *J. Am. Chem. Soc.* **2015**, *137*, 11996.

[19] D. Voiry, H. Yamaguchi, J. Li, R. Silva, D. C. Alves, T. Fujita, M. Chen, T. Asefa, V. B. Shenoy, G. Eda, M. Chhowalla, *Nat. Mater.* **2013**, *12*, 850.

[20] M. S. Burke, M. G. Kast, L. Trotochaud, A. M. Smith, S. W. Boettcher, *J. Am. Chem. Soc.* **2015**, *137*, 3638.

[21] K. Fominykh, J. M. Feckl, J. Sicklinger, M. Döblinger, S. Böcklein, J. Ziegler, L. Peter, J. Rathousky, E.-W. Scheidt, T. Bein, D. Fattakhova-Rohlfing, *Adv. Funct. Mater.* **2014**, *24*, 3123.

[22] S. Guo, S. Zhang, L. Wu, L. Sun, *Angew. Chem., Int. Ed.* **2012**, *51*, 11770.

[23] Y. Meng, W. Song, H. Huang, Z. Ren, S. Y. Chen, S. L. Suib, *J. Am. Chem. Soc.* **2014**, *136*, 11452.

[24] S. Peng, L. Li, X. Han, W. Sun, M. Srinivasan, S. G. Mhaisalkar, F. Cheng, Q. Yan, J. Chen, S. Ramakrishna, *Angew. Chem., Int. Ed.* **2014**, *53*, 12594.

[25] H. Wang, Y. Liang, Y. Li, H. Dai, *Angew. Chem., Int. Ed.* **2011**, *50*, 10969.

[26] J. Duan, S. Chen, M. Jaroniec, S. Z. Qiao, *ACS Nano* **2015**, *9*, 931.

[27] M. Gong, Y. Li, H. Wang, Y. Liang, J. Z. Wu, J. Zhou, J. Wang, T. Regier, F. Wei, H. Dai, *J. Am. Chem. Soc.* **2013**, *135*, 8452.

[28] Y. Liang, Y. Li, H. Wang, J. Zhou, J. Wang, T. Regier, H. Dai, *Nat. Mater.* **2011**, *10*, 780.

[29] H. W. Liang, W. Wei, Z. S. Wu, X. Feng, K. Mullen, *J. Am. Chem. Soc.* **2013**, *135*, 16002.

[30] Z. Y. Wu, X. X. Xu, B. C. Hu, H. W. Liang, Y. Lin, L. F. Chen, S. H. Yu, *Angew. Chem., Int. Ed.* **2015**, *54*, 8179.

[31] Y. Liang, H. Wang, J. Zhou, Y. Li, J. Wang, T. Regier, H. Dai, *J. Am. Chem. Soc.* **2012**, *134*, 35173.

[32] J. Masa, W. Xia, I. Sinev, A. Zhao, Z. Sun, S. Grutzke, P. Weide, M. Muhler, W. Schuhmann, *Angew. Chem., Int. Ed.* **2014**, *53*, 8508.

[33] J. Deng, P. Ren, D. Deng, X. Bao, *Angew. Chem., Int. Ed.* **2015**, *54*, 2100.

[34] Y. Yang, Z. Lun, G. Xia, F. Zheng, M. He, Q. Chen, *Energy Environ. Sci.* **2015**, *8*, 3563.

[35] M. Tan, C. K. Chua, D. Sedmidubsky, Z. C. Sofer, M. Pumera, *Phys. Chem. Chem. Phys.* **2016**, *18*, 1699.

[36] C. S. Lim, C. K. Chua, Z. Sofer, K. Klímová, C. Boothroyd, M. Pumera, *J. Mater. Chem. A* **2015**, *3*, 11920.

[37] X. Liu, W. Liu, M. Ko, M. Park, M. G. Kim, P. Oh, S. Chae, S. Park, A. Casimir, G. Wu, J. Cho, *Adv. Funct. Mater.* **2015**, *25*, 5799.

[38] Y. Hou, Z. Wen, S. Cui, S. Ci, S. Mao, J. Chen, *Adv. Funct. Mater.* **2015**, *25*, 872.

[39] X. Long, J. Li, S. Xiao, K. Yan, Z. Wang, H. Chen, S. Yang, *Angew. Chem., Int. Ed.* **2014**, *53*, 7584.

[40] X. Liu, M. Antonietti, *Adv. Mater.* **2013**, *25*, 6284.

[41] S. Yasuda, A. Furuya, Y. Uchibori, J. Kim, K. Murakoshi, *Adv. Funct. Mater.* **2016**, *26*, 738.

[42] Z. Li, Z. Xu, X. Tan, H. Wang, C. M. B. Holt, T. Stephenson, B. C. Olsen, D. Mitlin, *Energy Environ. Sci.* **2013**, *6*, 871.

[43] J. Liang, Y. Jiao, M. Jaroniec, S. Z. Qiao, *Angew. Chem., Int. Ed.* **2012**, *51*, 11496.

[44] Z.-H. Sheng, L. Shao, J. J. Chen, W. J. Bao, F. B. Wang, X. H. Xia, *ACS Nano* **2011**, *5*, 4350.

[45] H. X. Zhong, J. Wang, Y. W. Zhang, W. L. Xu, W. Xing, D. Xu, Y. F. Zhang, X. B. Zhang, *Angew. Chem., Int. Ed.* **2014**, *53*, 14235.

[46] T. Schiros, D. Nordlund, L. Palova, D. Prezzi, L. Zhao, K. S. Kim, U. Wurstbauer, C. Gutierrez, D. Delongchamp, C. Jaye, D. Fischer, H. Ogasawara, L. G. Pettersson, D. R. Reichman, P. Kim, M. S. Hybertsen, A. N. Pasupathy, *Nano Lett.* **2012**, *12*, 4025.

[47] Y. Zhao, R. Nakamura, K. Kamiya, S. Nakanishi, K. Hashimoto, *Nat. Commun.* **2013**, *4*, 2390.

[48] X. Long, G. Li, Z. Wang, H. Zhu, T. Zhang, S. Xiao, W. Guo, S. Yang, *J. Am. Chem. Soc.* **2015**, *137*, 11900.

[49] H. Liang, F. Meng, M. Caban-Acevedo, L. Li, A. Forticaux, L. Xiu, Z. Wang, S. Jin, *Nano Lett.* **2015**, *15*, 1421.

[50] A. Gupta, W. D. Chemelewski, C. Buddie Mullins, J. B. Goodenough, *Adv. Mater.* **2015**, *27*, 6063.

[51] Y. Li, W. Zhou, H. Wang, L. Xie, Y. Liang, F. Wei, J. C. Idrobo, S. J. Pennycook, H. Dai, *Nat. Nanotechnol.* **2012**, *7*, 394.

[52] Y. Chang, F. Hong, C. He, Q. Zhang, J. Liu, *Adv. Mater.* **2013**, *25*, 4794.

[53] W. Xia, R. Zou, L. An, D. Xia, S. Guo, *Energy Environ. Sci.* **2015**, *8*, 568.

[54] B. You, N. Jiang, M. Sheng, W. S. Drisdell, J. Yano, Y. Sun, *ACS Catal.* **2015**, *5*, 7068.

[55] J. Wang, K. Li, H. X. Zhong, D. Xu, Z. L. Wang, Z. Jiang, Z. J. Wu, X. B. Zhang, *Angew. Chem., Int. Ed.* **2015**, *54*, 10530.

[56] K. Xu, P. Chen, X. Li, Y. Tong, H. Ding, X. Wu, W. Chu, Z. Peng, C. Wu, Y. Xie, *J. Am. Chem. Soc.* **2015**, *137*, 4119.

[57] V. I. Birss, *J. Electrochem. Soc.* **1987**, *134*, 113.

[58] L. Cheng, W. Huang, Q. Gong, C. Liu, Z. Liu, Y. Li, H. Dai, *Angew. Chem., Int. Ed.* **2014**, *53*, 7860.

[59] X. Wang, Y. V. Kolen'ko, X. Q. Bao, K. Kovnir, L. Liu, *Angew. Chem., Int. Ed.* **2015**, *54*, 8188.